Binary star-polymer solutions: bulk and interfacial properties

2002 J. Phys.: Condens. Matter 14 12031

(http://iopscience.iop.org/0953-8984/14/46/311)

INSTITUTE OF PHYSICS PUBLISHING JOURNAL OF PHYSICS: CONDENSED MATTER

J. Phys.: Condens. Matter **14** (2002) 12031–12050 PII: S0953-8984(02)37674-4

Binary star-polymer solutions: bulk and interfacial properties

A J Archer[1], **C N Likos**[2] **and R Evans**[1]

[1] H H Wills Physics Laboratory, University of Bristol, Bristol BS8 1TL, UK
[2] Institut für Theoretische Physik II, Heinrich-Heine-Universität Düsseldorf, Universitätsstraße 1, D-40225 Düsseldorf, Germany

Received 5 June 2002
Published 8 November 2002
Online at stacks.iop.org/JPhysCM/14/12031

Abstract

Using an effective logarithmic–Gaussian pair potential that models the interaction between star polymers, we compare the hypernetted chain (HNC) and random phase approximations (RPA) for calculating the bulk structure (including the Fisher–Widom and Lifshitz lines), thermodynamic functions and phase diagram of a phase-separating binary fluid of star polymers, of two-arm length ratio 2:1. Thereby, the stars considered here are equivalent to linear chains in the mid-point representation of their effective interaction. We find that at densities where the star coronas overlap, the quasi-exact HNC and RPA give very similar results. Using a density functional approach, with a functional which generates the RPA, we calculate properties of the inhomogeneous binary fluid. We determine the surface tension and one-body density profiles at the free fluid–fluid interface. For states well removed from the critical point the profiles exhibit pronounced oscillations. For a purely repulsive planar wall potential that models the effective potential between a star polymer and a hard wall, we find a first-order wetting transition with the associated pre-wetting line.

(Some figures in this article are in colour only in the electronic version)

1. Introduction

When considering the problem of polymers in solution one is faced with a huge task if one starts the theoretical description from the monomeric degrees of freedom. The problem is greatly simplified if one can calculate an effective potential between the polymers, using a single position coordinate for each polymer (typically the centre of mass or the mid-chain monomer [1, 2]). The effective potential between the polymer chains is in general a many-body potential, and is density dependent. However, one often finds that a density-independent pair potential approximation for the interaction between the individual polymer chains is sufficient to give a reasonable description of the bulk structure and thermodynamics [1, 3, 4]. With this perspective, one is then able to bring to bear on the problem the machinery developed for simple

fluids, e.g. using integral equation theories for bulk fluid structure and thermodynamics [5]. A natural tool for calculating the properties of inhomogeneous fluids is density functional theory (DFT) [6]. In this paper we study a binary fluid of demixing star polymers. Star polymers are made up of a number of polymer chains (referred to as arms) covalently bonded to one common central core [7]. The arm number f, also called the *functionality*, is the physical property that allows one to interpolate between linear chains ($f = 1, 2$) and the colloidal limit $f \gg 1$ in which the stars resemble hard spheres [1, 8–10].

We choose a binary mixture of star polymers with $f = 2$ arms (i.e., polymers) with polymerization ratio $N_1{:}N_2 = 2{:}1$, in order to compare our results with those obtained for the binary Gaussian core model (GCM) [11, 12]. The GCM is a model for polymers in solution, modelling the effective potential between the centres of mass of the polymers by a repulsive Gaussian potential [1, 3, 13–18]. The GCM pair potential is defined as $v(r) = \epsilon \exp(-r^2/R^2)$ where for polymers at room temperature in an athermal solvent, $\epsilon \simeq 2k_BT$ and $R \simeq R_g$, the polymer radius of gyration. Note that the GCM potential remains finite for all separations r, representing the fact that in the underlying polymer system the centres of mass can completely overlap, even if the individual monomers cannot. In this paper we use an alternative representation for the chains: we choose their *central monomers* as generalized coordinates for a coarse-grained description and employ accordingly the effective interactions between central monomers in treating the polymers as ultrasoft colloids. In contrast to the centre-of-mass potential, the central-monomer effective potential does have a divergence as $r \to 0$, albeit a very weak, logarithmic one. This property, derived in the pioneering work of Witten and Pincus [19], stems from the scaling properties of the partition function of self-avoiding random walks and can be generalized to stars with an arbitrary number of arms [19]. Thus, the divergence is caused by the self-avoidance that restricts the number of available configurations of infinitely thin polymer threads and not by the direct monomer–monomer interaction. We choose to focus on star polymers with $f = 2$ arms in order to compare with the GCM because there is no difference between a star polymer with $f = 2$ arms and a simple polymer; hence we are simply calculating the properties of a binary polymer solution. In this case the star-polymer potential is an effective polymer pair potential between the central monomers on each of the two polymers. Since it is the same underlying system that these two effective potentials represent, these two different effective potentials should result in the same thermodynamic properties and phase behaviour.

The present paper is laid out as follows. In section 2, we describe the model binary star-polymer mixture. Then in section 3, by comparing with the more accurate HNC, we show that at sufficiently high densities the bulk structure and thermodynamics of the binary fluid can be approximated well by the simple RPA. The HNC is essentially exact for soft-core particles, giving results almost indistinguishable from simulation for sufficiently high densities of GCM particles [1, 17] and of star polymers with as many as 32 arms [20]. We calculate both the HNC and the RPA fluid–fluid coexistence curves in the total density–composition plane, and we find that at high densities, there is very little difference between the two. In the same section we also calculate the Fisher–Widom (FW) line, i.e., the line in the bulk phase diagram at which the asymptotic decay of the radial distribution functions (rdfs) $g_{ij}(r)$ crosses over from monotonic to damped oscillatory, and the Lifshitz lines, which separate regions where the partial structure factors $S_{ij}(k)$ have a maximum at $k = 0$ from those where there is a minimum at $k = 0$. In sections 4 and 5 we use a Helmholtz free energy functional which generates the RPA for bulk correlation functions to calculate the density profiles of the inhomogeneous binary fluid. We calculate the density profiles, along with the surface tension, for the planar interface between the demixed fluid phases in section 4, and then in section 5 we calculate the density profiles of the binary fluid at a planar wall with a purely repulsive wall–fluid potential

chosen to model the effective interaction between a star polymer and a hard wall. We find that there is a first-order wetting transition, with the associated pre-wetting line, whereby the fluid phase rich in the larger species completely wets the interface between the wall and the fluid phase rich in the smaller species. Finally, in section 6 we summarize and conclude.

2. The model mixture

In [21, 22], Jusufi *et al* proposed a repulsive logarithmic–Gaussian form for the effective potential between the centres of a pair (arm number $f < 10$) of star polymers in athermal solvents. This potential features a weak, $-\ln(r)$ divergence for small separations r, reflecting the fact that polymers are ultrasoft 'colloids'. The Gaussian decay pertains for large r and is identical in its functional form with the effective interaction between the centres of mass (the GCM) [3, 14–16]. Note that for arm numbers $f > 10$, the Gaussian decay of the pair potential is replaced by a Yukawa decay [8]. The multi-component generalization of the logarithmic–Gaussian potential reads as

$$\beta v_{ij}(r) = \frac{5}{18} f^{3/2} \begin{cases} -\ln\left(\dfrac{r}{\sigma_{ij}}\right) + \dfrac{1}{2\tau_{ij}^2\sigma_{ij}^2} & \text{for } r \leqslant \sigma_{ij}; \\ \dfrac{1}{2\tau_{ij}^2\sigma_{ij}^2} \exp[-\tau_{ij}^2(r^2 - \sigma_{ij}^2)] & \text{for } r > \sigma_{ij}, \end{cases} \tag{1}$$

where σ_{ij} is the corona diameter and τ_{ij} is a parameter of order $1/R_{ij}$ where R_{ij} is the radius of gyration [21] and $\beta = 1/k_BT$. In the present work we choose to set the arm number $f = 2$, so that the star-polymer pair potential (1) is equivalent to the effective potential between the central monomers on a polymer chain, and we can therefore compare the present 'central-monomer' representation with the 'centre-of-mass' effective potential in earlier work [11, 12]. The arm number f only appears in the prefactor of the pair potential (1), so we expect that all results presented will be qualitatively correct for $f < 10$. For the parameters of interaction between unlike species in a binary mixture, $i, j = 1, 2$, we choose the mixing rules

$$\sigma_{12} = \tfrac{1}{2}(\sigma_{11} + \sigma_{22}) \tag{2}$$

and

$$\frac{1}{\tau_{12}^2} = \frac{1}{2}\left(\frac{1}{\tau_{11}^2} + \frac{1}{\tau_{22}^2}\right). \tag{3}$$

The additive rule, equation (2), is roughly what we expect for the effective cross-interaction corona diameter σ_{12}. The precise value chosen for σ_{12} does not have much of an effect on the overall phase behaviour of the system; it simply sets the critical point total bulk density, ρ_c, of the binary phase-separating mixture. It thereby plays a role similar to ϵ_{12} for the GCM in locating the critical point [11, 16, 23]. The rule described by equation (3) plays a more significant role in determining the behaviour of the binary fluid. Since $\tau_{ij} \simeq 1/R_{ij}$, we use equation (3) to determine τ_{12}, because this relation has been found in simulations when considering the effective interaction between the centres of mass of the polymers [14, 16] (as opposed to the central monomer in the present work), and is what was used in the previous work [11, 12] on the inhomogeneous binary GCM.

In order to make a comparison with our earlier work [11, 12], we choose $\sigma_{22}/\sigma_{11} = 0.665$ which is equivalent to a binary mixture of polymers of polymerization ratio[3] $N_1{:}N_2 = 2{:}1$. In [21], it was found that $\tau_{ii} = 1.03/\sigma_{ii}$ gives excellent agreement with simulation results

[3] This arises from the scaling law $R \sim N^{\nu}$ connecting the spatial extent R of a self-avoiding polymer with its degree of polymerization N, using the value $\nu = 3/5$ of the Flory exponent.

and, in addition, it brings about the best agreement for the second virial coefficient of polymer solutions. Using these ratios along with equations (2) and (3), the model mixture parameters are completely determined.

3. Bulk structure and phase diagram

We consider a system consisting of M_1 long and M_2 short chains enclosed in the volume V. Accordingly, we define the partial densities $\rho_i = M_i/V$, $i = 1, 2$, of the components, as well as the total density $\rho = \rho_1 + \rho_2$ and the concentration of the small component, $x = \rho_2/\rho$. Due to the athermal character of the solvent, the effective interactions are purely entropic, i.e., they scale linearly with k_BT and the thermal energy is the only energy scale of the problem, as is clear from equation (1). Thereby, the temperature drops out of the problem as an irrelevant variable and the thermodynamic space of the system is spanned by the partial densities or equivalently the pair (x, ρ).

In order to determine the bulk structure of the binary fluid we use the hypernetted chain (HNC) closure for direct pair correlation function, $c_{ij}(r)$, in terms of the pair correlation function $h_{ij}(r) = g_{ij}(r) - 1$ in the Ornstein–Zernike (OZ) equation [5], which, for a multi-component fluid, is

$$c_{ij}(r) = -\beta v_{ij}(r) + h_{ij}(r) - \ln[1 + h_{ij}(r)]. \tag{4}$$

We expect the HNC to be almost exact for describing the bulk structure of these soft-core particles at densities where the cores of the particles start to overlap ($\rho\sigma^3 \gtrsim 1.0$). This expectation is corroborated on the one hand from the known fact that for the one-component GCM the HNC results are indistinguishable from the simulation results at these densities [1, 16–18] and on the other hand by the finding that the HNC at high densities exhibits excellent agreement with simulation for a pure star-polymer fluid with functionality $f = 32$ [20][4].

We define the partial structure factors $S_{ij}(k)$, $i, j = 1, 2$, of the mixture as

$$\begin{aligned} S_{11}(k) &= 1 + \rho_1 \hat{h}_{11}(k); \\ S_{22}(k) &= 1 + \rho_2 \hat{h}_{22}(k); \\ S_{12}(k) &= \sqrt{\rho_1\rho_2}\,\hat{h}_{12}(k), \end{aligned} \tag{5}$$

where $\hat{h}_{ij}(k)$ denotes the Fourier transform (FT) of $h_{ij}(r)$. In addition, we consider later the concentration–concentration structure factor $S_{cc}(k)$, given by [24, 25]

$$S_{cc}(k) = (1 - x)^2 S_{11}(k) + x^2 S_{22}(k) - 2x(1 - x)S_{12}(k). \tag{6}$$

In figure 1 we show the HNC partial structure factors for the binary fluid, comparing also with the much simpler random phase approximation (RPA), which is given by $c_{ij}(r) = -\beta v_{ij}(r)$. The RPA closure to the OZ equations becomes more accurate as the density is increased and is very reliable for interaction potentials that diverge slowly at the origin or are bounded there [18, 26]. Indeed, the RPA is in principle a good candidate for use in examining the structure of uniform *and* non-uniform fluids, when the condition $\int \mathrm{d}^3 r\, v_{ij}(r) < \infty$ is fulfilled [10, 26]. For the case of the GCM one- and two-component systems, the validity of the RPA has already been explicitly confirmed [11, 16, 17]. For non-bounded but slowly diverging interactions, the RPA is a good approximation at least for the thermodynamics, but it can also be accurate for the structure when the prefactor of the weakly diverging potential is small [26]. For the case at hand, the prefactor of the logarithmically diverging potentials is

[4] Due to the $f^{3/2}$-prefactor of the star–star potential, the $f = 32$ effective interaction is much steeper than the $f = 2$ one. The success of the HNC for this steeper interaction, then, guarantees its validity for the much softer interaction considered here.

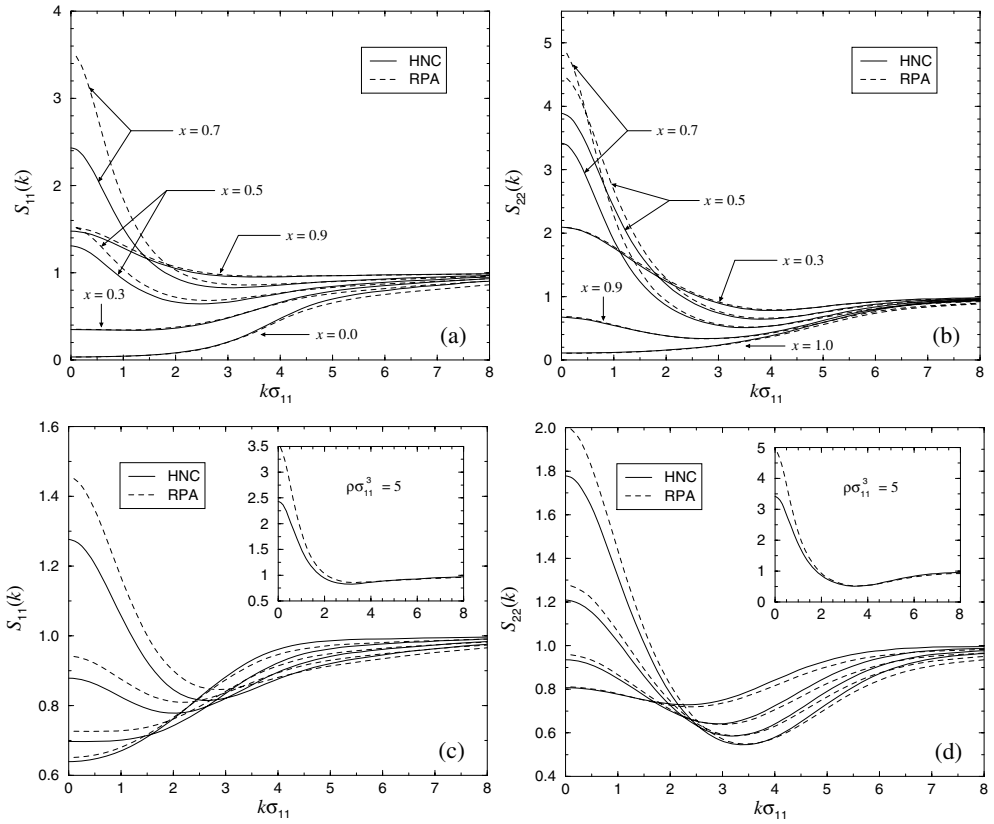

Figure 1. The partial structure factors, calculated along two different thermodynamic paths in the (x, ρ) plane of the star-polymer mixture obtained from the HNC (solid curves) and RPA (broken curves). (a) $S_{11}(k)$ for fixed total density $\rho\sigma_{11}^3 = 5$ and for different concentrations x of species 2, as indicated on the plot. (b) Results for $S_{22}(k)$ along the same path. (c) $S_{11}(k)$ at fixed concentration $x = 0.7$ and for increasing total densities; from bottom to top $\rho\sigma_{11}^3 = 1$, 2, 3 and 4. The inset shows the result for $\rho\sigma_{11}^3 = 5$, a point lying close to the RPA critical (consolute) point $(x_c, \rho_c\sigma_{11}^3) = (0.7095, 5.716\,28)$; see also figure 3. The inset axes have the same labels as those of the main plot. (d) As (c), but for the partial structure factor $S_{22}(k)$. Note that in all plots the $k \to 0$ limits predicted by the RPA are larger than those from the HNC and the discrepancies become more pronounced in the neighbourhood of the RPA critical point. At the critical point $S_{11}(k = 0)$ and $S_{22}(k = 0) \to +\infty$, whereas $S_{12}(k = 0) \to -\infty$.

indeed small, $(5/18)f^{3/2} = 0.786$ for $f = 2$, and thus the RPA should be valid at sufficiently high densities; a hypothesis that we confirm.

The comparison in figure 1 reveals that the HNC and the RPA yield very similar structure factors. The discrepancies between the two occur mostly for small k-values and are most pronounced in the neighbourhood of the critical point. The existence of a spinodal (and thus of phase separation) in the mixture is witnessed in both the HNC and the RPA by the increase (and eventual divergence) of the structure factors at $k = 0$. As we move along a path of fixed concentration x increasing the total density ρ, the RPA structure factors are seen to diverge earlier than the HNC ones, a feature pointing to the fact that the RPA coexistence region will be broader than the one predicted by the HNC approach. In addition, the fluid structure factors are quite similar to the equivalent GCM partial structure factors $S_{ij}(k)$. The reason for this is that in

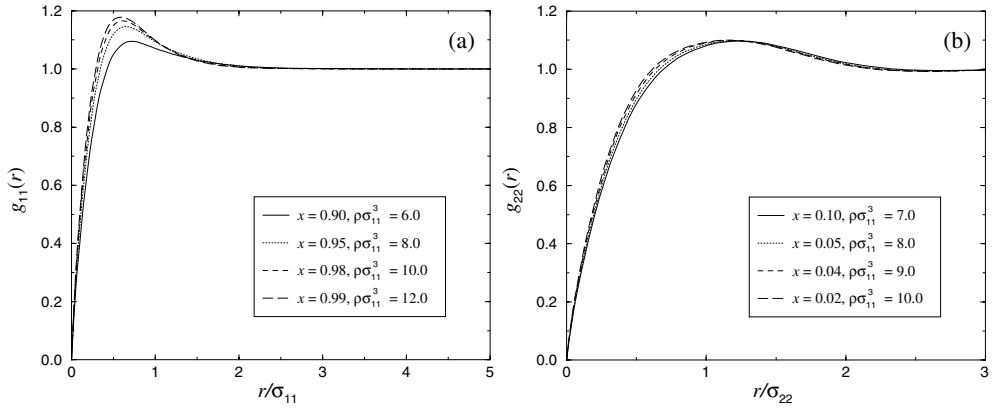

Figure 2. The HNC rdfs $g_{ii}(r)$ of the minority phases at high total densities. (a) Large particles, $g_{11}(r)$, and (b) small particles, $g_{22}(r)$.

calculating $S_{ij}(k)$, one Fourier transforms the pair potentials, $v_{ij}(r)$, which involves integrals of the form $\int \mathrm{d}r\, r \sin(kr) v_{ij}(r)$. Therefore, the weak divergence of the pair potential $v_{ij}(r)$ at small r has little effect because it is suppressed by the multiplication with $r \sin(kr)$. It is rather the fashion in which $v_{ij}(r)$ decays as $r \to \infty$ that has greater influence on the structure and the thermodynamics of the mixture [3, 27]: as we show later, the quantity $\hat{v}_{ij}(0) \propto \int \mathrm{d}r\, r^2 v_{ij}(r)$ enters into the RPA equation of state and is thus decisive in determining the phase boundaries.

We now turn our attention to the partial rdfs $g_{ij}(r)$, $i, j = 1, 2$, in particular at high densities and close to the borderlines $x = 0$ and 1. In these cases, the HNC approach and the RPA yield practically identical results, so we examine the HNC results here. As shown in figure 2, we find a signature of 'clustering' in the rdfs $g_{ij}(r)$ of the minority phase, i.e., the development of a pronounced maximum. This feature was also found for the GCM [23], but there the maxima are at $r = 0$. In the present model, $g_{ij}(r)$ does not have a maximum at $r = 0$, because our potentials have the logarithmic divergence at $r = 0$. Rather, the minority phase rdfs $g_{ii}(r)$, have a peak in the range $\sigma_{ii}/2 \lesssim r \lesssim \sigma_{ii}$. Since σ_{ii} is the diameter of the i-species and r denotes distances between the central monomers, this corresponds, roughly, to the centres of mass accumulating in one region and the polymers in the minority phase building clusters. There is therefore good agreement between the centre-of-mass and the central-monomer representation. Moreover, this clustering effect, which is more pronounced for the large polymers, is an additional signature of phase separation.

Next we consider the overall phase behaviour of the mixture and make a comparison between the binodal obtained from the HNC equation of state and that obtained from the particularly simple RPA equation of state. The simplest mean-field Helmholtz free energy functional for the mixture reads as

$$\mathcal{F}[\{\rho_i\}] = \mathcal{F}_{id}[\{\rho_i\}] + \tfrac{1}{2} \sum_{ij} \int \mathrm{d}^3 r_1 \int \mathrm{d}^3 r_2\, \rho_i(\boldsymbol{r}_1) \rho_j(\boldsymbol{r}_2) v_{ij}(|\boldsymbol{r}_1 - \boldsymbol{r}_2|) \qquad (7)$$

where $\mathcal{F}_{id}$ is the ideal gas part. This functional replaces all excess free energy contributions with the mean-field interaction terms that are bilinear in the density profiles $\rho_i(\boldsymbol{r})$ of the components. Such an approximation is expected to be accurate for the system at hand, which is deprived of hard cores and of significant short-range, excluded-volume correlations, in particular at high densities when the particles interact with a very large number of 'neighbours'. Recalling that

the two-body direct correlation functions are given by

$$c_{ij}^{(2)}(\boldsymbol{r}_1, \boldsymbol{r}_2) = -\frac{\beta\delta^2(\mathcal{F}[\{\rho_i\}] - \mathcal{F}_{id}[\{\rho_i\}])}{\delta\rho_i(\boldsymbol{r}_1)\,\delta\rho_j(\boldsymbol{r}_2)} \tag{8}$$

it follows that

$$c_{ij}^{(2)}(\boldsymbol{r}_1, \boldsymbol{r}_2) = c_{ij}^{(2)}(|\boldsymbol{r}_1 - \boldsymbol{r}_2|) = -\beta v_{ij}(|\boldsymbol{r}_1 - \boldsymbol{r}_2|) \tag{9}$$

which is the standard RPA approximation. In the bulk mixture the densities are constants, $\rho_i(\boldsymbol{r}) = \rho_i$. Expressing these in terms of the total density ρ and the composition variable x, we can write the bulk Helmholtz free energy per particle, $\tilde{f}$, as [11, 16]

$$\tilde{f}(\rho, x) = \tilde{f}_{id}(\rho, x) + \tfrac{1}{2}\rho[(1-x)^2\hat{v}_{11}(0) + 2x(1-x)\hat{v}_{12}(0) + x^2\hat{v}_{22}(0)]. \tag{10}$$

The ideal contribution, $\tilde{f}_{id}(\rho, x)$, contains the ideal free energy of mixing, $\beta^{-1}\{x\ln(x) + (1-x)\ln(1-x)\}$, as well as an irrelevant term with linear-in-ρ dependence. $\hat{v}_{ij}(0)$ is the $q = 0$ limit of the FT of the pair potential:

$$\hat{v}_{ij}(0) = \int \mathrm{d}^3 r\; v_{ij}(r). \tag{11}$$

Note that equation (10) is equivalent to calculating $\tilde{f}$ from the compressibility route. We now Legendre transform to obtain the Gibbs free energy per particle $g = \tilde{f} + Pv$, where $v = 1/\rho$ is the volume per particle and the pressure is given as $P = -(\partial\tilde{f}/\partial v)_x$. The common-tangent construction on g yields the binodal which is plotted along with the spinodal in figure 3. We find that the binodal has a very similar shape to that found for the GCM [11], since they have the same form for the bulk Helmholtz free energy (10), but they differ in where they locate the critical point. For the present star-polymer model we find the critical point at $\rho_c\sigma_{11}^3 = 5.7$ where the star-corona diameter $\sigma_{11} \simeq 1.32R_{11}^g$, with R_{11}^g the radius of gyration [21, 28]. On the other hand, for the GCM studied in [11] we found $\rho_c R_{11}^3 = 5.6$ with radius $R_{11} \simeq R_{11}^g$.

We also determined the HNC phase diagram. The HNC closure breaks down before a spinodal is reached, as is well known from previous studies [29, 30]. However, this poses no difficulties in calculating the HNC binodals[5]. For all points in the region where the HNC converges, we calculate the pressure P and partial chemical potentials μ_1, μ_2 on a grid. For the HNC, this calculation is local, i.e., one needs no thermodynamic integration to obtain μ_1 and μ_2 [23, 31]. From μ_1 and μ_2, the Gibbs free energy per particle $g = (1-x)\mu_1 + x\mu_2$ is readily obtainable. We perform a 2D interpolation of the pressure results to obtain $P(x, \rho)$ as a function of two variables for any x and ρ, and on this surface we determine the isobar curves $P =$ constant. We then draw the Gibbs free energy along the isobars to obtain $g_P(x)$, where the subscript now denotes that P is fixed. For those pressures for which $g_P(x)$ is a convex function of x, the system is in a single (mixed) state. For those for which it is not, the common-tangent construction determines the coexistence concentrations and densities. The region in which the HNC has no solutions presents no difficulties. For the isobars that intersect the borderline of this region, we simply have $g_P(x)$ with two 'branches' on either side of the prohibited domain and we perform the common-tangent construction on those.

The HNC binodal is plotted in figure 3 along with the RPA one. It can be seen that there is very good agreement between the two. The RPA binodal is slightly broader but the discrepancies become quickly suppressed in moving away from the critical point. If one interprets the total density as an 'inverse temperature' and the concentration as a 'density' of a hypothetical one-component system, then the phase diagram can be regarded as that

[5] We found, in fact, that the locus of points on which the HNC fails to converge is a curve that runs close to the RPA spinodal and in the U-shaped region in the high-density part of this curve the HNC has no solutions.

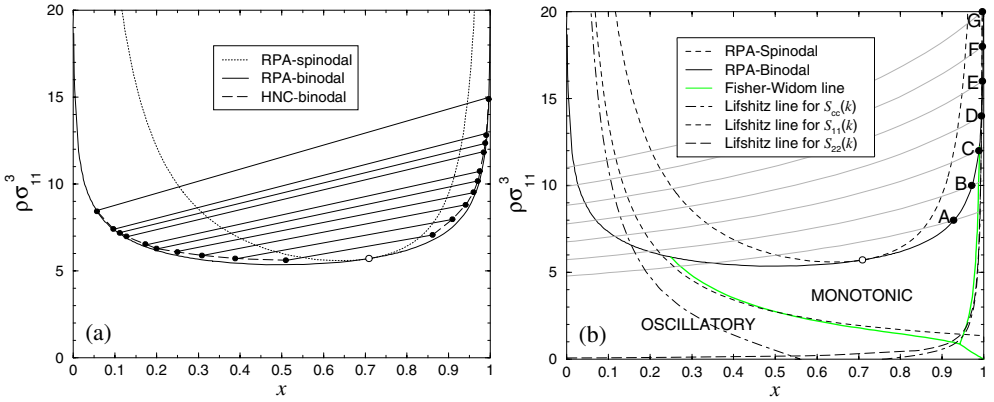

Figure 3. (a) The RPA spinodal and binodal lines for the star-polymer mixture (dotted and solid curves) along with the HNC binodal (dashed curve). x is the concentration of species 2, the smaller component. The straight segments denote HNC tie lines between coexisting fluid phases whose coordinates are given by the closed circles at their ends. (b) The RPA phase diagram along with the FW line (light solid curve) and the Lifshitz curves of the various structure factors. The left-hand branch of the FW line lies close to the Lifshitz curve for $S_{11}(k)$ (short-dashed curve) while the right-hand branch lies close to the Lifshitz curve for $S_{22}(k)$ (long-dashed curve). The dash–dotted line is the Lifshitz line for $S_{cc}(k)$. The points A–G on the right-hand branch of the binodal are located at total densities $\rho\sigma_{11}^3 = 8$, 10, 12, 14, 16, 18 and 20, at which the free interface density profiles will be calculated in section 4. The grey lines are RPA isobars through the points A–G and their intersections with the left-hand branch of the binodal yield the state points coexisting with A–G. The open circle denotes the RPA critical point.

corresponding to 'liquid–gas' coexistence. The RPA is then equivalent to the mean-field approximation, which usually delivers critical temperatures *higher* than the true result. That the RPA critical density is *lower* than the HNC one can be explained by means of this analogy. The largest discrepancies between HNC and RPA occur close to the critical point but these are less than 10% for the location of the binodal on the density axis. Otherwise, the remarkable accuracy of the RPA can be understood from the fact that the phase separation for our binary fluid occurs at a sufficiently high density that the differences between the RPA and HNC routes to the bulk structure and thermodynamics are indeed very small. We demonstrate this in figure 4, where we show representative results for the chemical potentials and the pressure obtained by the two approaches. We note that Finken *et al* [23] have also made comparisons between the RPA and HNC results for the binodal in the case of a binary mixture of repulsive GCM particles. They report larger differences between the two theories than we find here. At present it is not clear why the differences should be larger for GCM particles than for the (very similar) logarithmic–Gauss potentials that we consider in the present study.

More detailed information about the nature of the interparticle correlations in the mixture can be obtained by investigating the FW line [32]. The FW line is determined by the asymptotic decay, $r \to \infty$, of the total pairwise correlation functions $h_{ij}(r)$. It is the locus of points in the phase diagram at which the ultimate decay of the pair correlation functions crosses over from monotonic (OZ-like) to damped oscillatory. The genesis of the FW line in mixtures is described in [11, 33]. In Fourier space the OZ equations for $h_{ij}(r)$ in a two-component liquid are

$$\hat{h}_{ij}(q) = \frac{N_{ij}(q)}{D(q)} \tag{12}$$

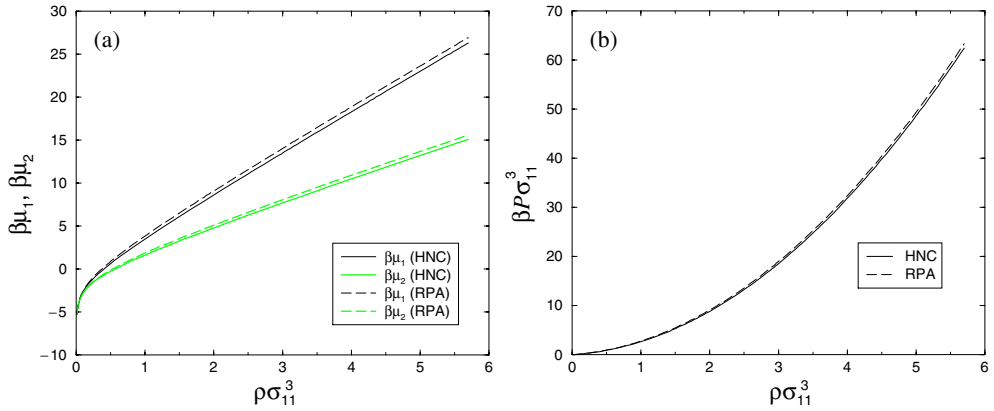

Figure 4. Comparison of the HNC and RPA results for the partial chemical potentials (a) and the total pressure (b), at fixed concentration $x = 0.5$ and increasing total density ρ.

where the numerators are given by

$$N_{11}(q) = \hat{c}_{11}(q) + \rho_2[\hat{c}_{12}^2(q) - \hat{c}_{11}(q)\hat{c}_{22}(q)];$$
$$N_{22}(q) = \hat{c}_{22}(q) + \rho_1[\hat{c}_{12}^2(q) - \hat{c}_{11}(q)\hat{c}_{22}(q)]; \tag{13}$$
$$N_{12}(q) = \hat{c}_{12}(q),$$

and the denominator is

$$D(q) = [1 - \rho_1\hat{c}_{11}(q)][1 - \rho_2\hat{c}_{22}(q)] - \rho_1\rho_2\hat{c}_{12}^2(q), \tag{14}$$

where $\hat{c}_{ij}(q)$ is the FT of $c_{ij}(r)$. Inverting the FT, and noting that $\hat{h}_{ij}(q)$ is even, we can write

$$rh_{ij}(r) = \frac{1}{4\pi^2 \mathrm{i}} \int_{-\infty}^{\infty} \mathrm{d}q\, q \frac{N_{ij}(q)}{D(q)} \exp(\mathrm{i}qr) \tag{15}$$

which can be evaluated by contour integration [33]. Using the RPA approximation for the direct pair correlation function, $\hat{c}_{ij}(q) = -\beta\hat{v}_{ij}(q)$, greatly facilitates the calculation of the FW line, since the FTs $\hat{v}_{ij}(q)$ are analytic (see the appendix). The singularities of $\hat{h}_{ij}(q)$ are simple poles. Choosing an infinite radius semi-circle in the upper half of the complex plane, we obtain

$$rh_{ij}(r) = \frac{1}{2\pi} \sum_n R_n^{ij} \exp(\mathrm{i}q_n r) \tag{16}$$

where R_n^{ij} is the residue of $qN_{ij}(q)/D(q)$ for the nth pole at $q = q_n$. The q_n are solutions of $D(q_n) = 0$ and there are normally an infinite number of poles. If a pole lies on the imaginary axis, $q_n = \mathrm{i}\alpha_0$, it contributes a pure exponential term of the form $\exp(-\alpha_0 r)$ to the sum in equation (16). Poles lying off the imaginary axis occur in conjugate pairs $q_n = \pm\alpha_1 + \mathrm{i}\tilde{\alpha}_0$ and such a pair contributes a damped oscillatory term of the form $\exp(-\tilde{\alpha}_0 r)\cos(\alpha_1 r - \theta)$ to the sum in equation (16). The longest range decay of $h_{ij}(r)$ is determined by the pole or the conjugate pair of poles with the smallest imaginary part. If $\alpha_0 < \tilde{\alpha}_0$, the longest range decay is monotonic (pure exponential); otherwise it is damped oscillatory. Since all three $\hat{h}_{ij}(q)$ have a common denominator $D(q)$, it follows that all three $h_{ij}(r)$ decay ultimately with the same decay length and wavelength. The residues do depend on the particular species but these determine only the amplitudes and phases of the ultimate decay [33, 35, 36]. Similar arguments [33] apply for the one-body density profiles in a binary mixture and the same quantities α_0, $\tilde{\alpha}_0$ and α_1 determine

the ultimate decay into bulk of the one-body density profiles at interfaces. The FW line is the crossover line in the phase diagram where $\alpha_0 = \tilde{\alpha}_0$. The FW line for the present mixture is displayed in figure 3. We find that the FW line is almost exactly the same in shape and location in the phase diagram as that found, also using the RPA, for the binary GCM corresponding to a 2:1 length ratio mixture of polymers [11]. We also find the same cusp in the FW line (bottom right-hand corner, figure 3(b)) and the new line found in [11]. The latter denotes the crossover from oscillatory decay with one wavelength, corresponding to the length scale associated with one of the particle species, to oscillatory decay with another wavelength, determined by the size of the other species of particles. Because the RPA binodal and FW lines are so similar in the present model to those found for the binary GCM [11], we expect the trends found as particle size asymmetry was varied in the GCM to carry over to the present model, i.e., as the size asymmetry is increased, the location of the critical point should move towards the side of the phase diagram rich in the smaller species and the cusp in the FW line should move to this side also. Note also that the pole determining the asymptotic decay of $g_{ij}(r)$ also sets the common bulk correlation length: $\xi = 1/\alpha_0$ [33]. It is possible to calculate the leading pole from numerical solutions for the HNC [36]; however, we expect the asymptotic decay to be very well captured by the RPA, and the dominant HNC pole to be very similar in value to that obtained from the analytically tractable RPA, as was the case for the one-component GCM [11, 37].

The Lifshitz line [38, 39][6] separates the region in the phase diagram in which $S_{ij}(k)$ has a local maximum at $k = 0$ (as occurs near a critical point or spinodal) from that in which it has a local minimum at $k = 0$. Making a small-k expansion of the partial structure factors:

$$S_{ij}(k) = a(\rho, x) + b(\rho, x)k^2 + \mathrm{O}(k^4), \tag{17}$$

and examining the sign of the term $b(\rho, x)$, one sees that the Lifshitz line is the locus of points $b(\rho, x) = 0$. The Lifshitz lines for two of the partial structure factors are displayed in figure 3 and their shapes are similar to those of branches of the FW line. This is because their locations are driven by the proximity of the spinodal, which forces $S_{11}(k)$ and $S_{22}(k)$ to have maxima at $k = 0$. These maxima survive as long as the pure imaginary pole (away from the spinodal) is the dominant one. Close to the crossover to damped oscillatory decay in $h_{ij}(r)$, at the FW line, the maximum turns into a minimum. Hence the Lifshitz and the FW lines are closely related to one another but they are not identical. Since phase separation in liquid mixtures is driven by concentration fluctuations, it is natural to examine the Lifshitz line for the concentration–concentration structure factor $S_{cc}(k)$ defined in equation (6). As can be seen in figure 3, the domain enclosed by the Lifshitz line, in which $S_{cc}(k = 0)$ is a maximum, is broader than the domain in which both $S_{11}(k = 0)$ and $S_{22}(k = 0)$ are local maxima. This is the effect of the term $-2x(1 - x)S_{12}(k)$. In fact, the Lifshitz line for $S_{cc}(k = 0)$ does not close: even at very low densities, there survives a domain, in this case $0.55 \lesssim x \lesssim 0.77$, in which $S_{cc}(k)$ has a small maximum at $k = 0$. The Lifshitz line for $S_{12}(k)$ runs similarly to the one for $S_{11}(k)$, but the regions it separates are inverted with respect to the ones for $S_{11}(k)$ and $S_{22}(k)$: above the Lifshitz line for $S_{12}(k)$, the latter has a local minimum at $k = 0$ and below it a local maximum[7], whereas the situation is inverted for the other two.

[6] We note that for microemulsions both the Lifshitz and the FW line are used to signify the crossover from the 'sponge phase' to the 'random phase' (there is no sharp thermodynamic transition between the two; hence one resorts to structural criteria) [38, 39]. The locations of the two lines in the phase diagram are related, as in the present fluid. We note also that in the microemulsion literature the FW line is referred to as the disorder line [38], the latter terminology being the common one for Ising models [35, 40].

[7] Note that at the spinodal, $S_{12}(k = 0)$ diverges to minus infinity, not to plus infinity as do $S_{11}(k = 0)$ and $S_{22}(k = 0)$.

4. The free fluid–fluid interface

In this section we calculate the inhomogeneous one-body density profiles of the fluid at the planar interface between two coexisting phase-separated liquid phases and the corresponding surface tension γ, using the same DFT (7) as generates the RPA. We work with the grand potential functional

$$\Omega_V[\{\rho_i\}] = \mathcal{F}[\{\rho_i\}] - \sum_i \int \mathrm{d}^3 r\, (\mu_i - V_i(\boldsymbol{r}))\rho_i(\boldsymbol{r}), \tag{18}$$

where μ_i is the chemical potential of species $i = 1, 2$, and determine the free interface density profiles by setting the external potentials $V_i(\boldsymbol{r}) = V_i(z) = 0$. Within the present mean-field approach the resulting profiles $\rho_i(z)$, with z normal to the interface, are non-trivial, i.e., the interface has a finite width. Minimizing (18) and using (7) for $\mathcal{F}[\{\rho_i\}]$ yields a pair of coupled Euler–Lagrange equations for the profiles. Due to the planar symmetry these can be reduced to a pair of one-dimensional equations:

$$\mu_i - V_i(z) = \mu_{i,id}(\rho_i(z)) + \sum_j \int \mathrm{d}z'\, \rho_j(z')\tilde{v}_{ij}(|z - z'|), \qquad \text{for } i,\, j = 1, 2 \tag{19}$$

where the ideal gas chemical potential $\mu_{i,id}(\rho_i) = \beta^{-1} \ln(\Lambda_i^3 \rho_i)$ (Λ_i is the thermal de Broglie wavelength) and

$$\tilde{v}_{ij}(|z - z'|) = \int_{-\infty}^{\infty} \mathrm{d}x \int_{-\infty}^{\infty} \mathrm{d}y\, v_{ij}(|\boldsymbol{r} - \boldsymbol{r}'|). \tag{20}$$

Equations (19) can be solved self-consistently for the density profiles of the two species. We find results very similar to those for the binary GCM [11]. Once again, the weak divergence of the pair potential $v_{ij}(r)$ has little effect. When (1) is substituted into (20) we find that $\tilde{v}_{ij}(z)$ is finite for all z: on integrating over the x–y plane the $-\ln(r)$ divergence in $v_{ij}(r)$ yields a term $\sim z^2 \ln(z)$, which is finite as $z \to 0$. In fact $\tilde{v}_{ij}(z)$ resulting from equations (1) and (20) has a very similar shape to that resulting from substituting $v_{ij}(r) = \epsilon_{ij} \exp(-r^2/R_{ij}^2)$ (GCM) into (20). The resulting density profiles for the coexisting states marked in figure 3(b) are displayed in figure 5. We find pronounced oscillations in the density profile of the larger species, $\rho_1(z)$, for states well removed from the critical point, similar to those that we found for the GCM [11]. For states B–G (see the phase diagram, figure 3) both density profiles $\rho_1(z)$ and $\rho_2(z)$ exhibit non-monotonic decay into the bulk phase which is rich in species 1. On the other side of the interface, approaching the bulk phase rich in species 2, magnification shows that both $\rho_1(z)$ and $\rho_2(z)$ are non-monotonic for states E–G. For state A, closer to the critical point, there is no sign of oscillations on either side of the interface.

Within the context of DFT it is the location of the FW line that determines the crossover from monotonic to damped oscillatory decay in the free interface density profiles [11, 35, 41]. On moving along the binodal away from the critical point, and crossing the intersection with the FW line, there are bulk states (on the binodal) at which the pair correlation functions, $h_{ij}(r)$, decay in a damped oscillatory fashion. Since it is the same pole in the structure factors that determines the asymptotic decay of the one-body density profiles, $\rho_i(r)$, for these states on the oscillatory side of the FW line one should expect damped oscillatory decay of $\rho_i(r)$ into the bulk phase. For the present model the FW line intersects the binodal on both sides, so when both bulk coexisting states are on the oscillatory side of the FW line, then the asymptotic decay of the density profiles will be damped oscillatory on both sides of the interface [11].

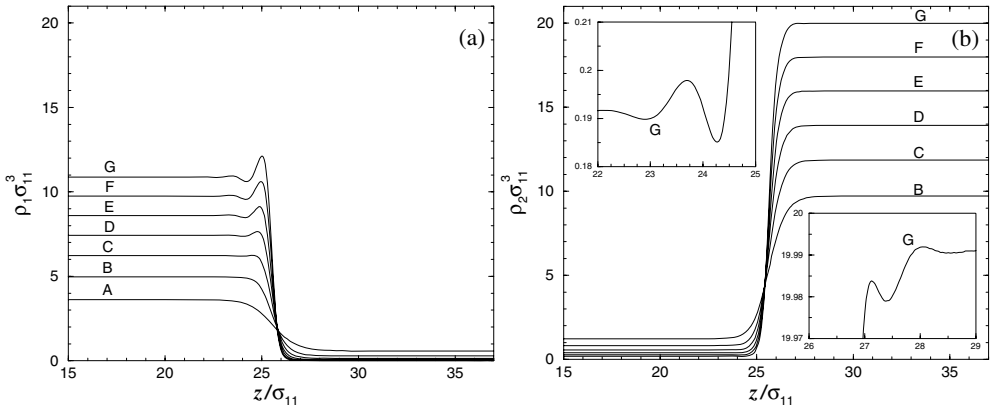

Figure 5. The fluid–fluid interface density profiles, calculated at states A–G in the phase diagram (see figure 3(b)). State A lies near the critical point and state G, for which the interface is much sharper, far away from the critical point. These states correspond to total bulk densities $\rho\sigma_{11}^3 = 8$, 10, 12, 14, 16, 18 and 20 in the phase rich in species 2. (a) Density profiles of species 1, the larger species. (b) Density profiles of species 2. The insets show magnified regions for state G. Note the oscillations on both sides of the interface.

Having calculated the equilibrium free interface density profiles we can determine the surface tension, which is defined as the excess grand potential per unit area and can be written as

$$\gamma = \int_{-\infty}^{\infty} \mathrm{d}z\,(P + \omega(z)), \tag{21}$$

where P is the bulk pressure at coexistence and $\omega(z)$ is the grand potential density obtained from equations (7) and (18) with $V_i(z) = 0$. The reduced tension $\gamma^* = \beta\gamma\sigma_{11}^2$ is plotted in figure 6 for the interfaces corresponding to figure 5. We have chosen to plot γ^* versus the order parameter $(\rho_1^{\mathrm{A}} - \rho_1^{\mathrm{B}})\sigma_{11}^3$, where ρ_1^{A} is the bulk density of species 1 in phase A, rich in species 1, and ρ_1^{B} is the same quantity in phase B, poor in species 1 [11, 42]. Mean-field arguments imply that γ^* should vanish as $(\rho_1^{\mathrm{A}} - \rho_1^{\mathrm{B}})^3$ on approaching the critical point and this is confirmed by our numerical results (see the inset to figure 6).

We can obtain an estimate for the surface tension of a phase-separated mixture of 'real' star polymers by choosing $\gamma^* = 5$, corresponding to a state well removed from the critical point, and setting $T = 300$ K and $\sigma_{11} = 20$ nm. We find $\gamma = 52\ \mu\mathrm{N\,m^{-1}}$, the same as for the GCM [11]. This tension is one order of magnitude greater than that calculated and measured for a colloid–polymer mixture [41, 42], but is two orders of magnitude smaller than the tensions of simple atomic fluids near their triple points.

The numerical values of γ^* determine whether we can expect to observe oscillatory density profiles in a more accurate treatment of the free interface. As the present mean-field functional does not include the effects of capillary-wave fluctuations, one needs to make an estimate of these fluctuation effects on oscillatory structure [6]. Oscillatory free interface density profiles were found for the GCM [11], and also in an earlier DFT treatment of the free interface [35]. For thermodynamic states well away from the bulk critical point, Evans *et al* [35] found much smaller oscillations on the liquid side of the planar liquid–vapour density profiles for a one-component square-well fluid. Later Brader *et al* [41] found pronounced oscillations with a similar relative amplitude to those in the present model, on the colloid-rich side of the free interface, in a DFT treatment of a model colloid–(ideal) polymer mixture in which colloid–colloid and colloid–polymer interactions are hard-sphere-like. Oscillatory profiles

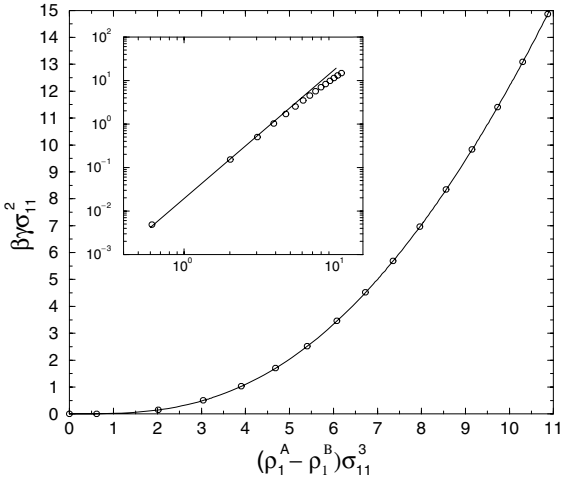

Figure 6. The reduced surface tension, $\gamma^* = \beta\gamma\sigma_{11}^2$, at the planar free interface, plotted against the order parameter $(\rho_1^A - \rho_1^B)\sigma_{11}^3$, the density difference in species 1 between the two phases, which vanishes at the critical point. The line joining the data points is a guide to the eye. Inset: a double-logarithmic plot of the same quantities, demonstrating the power-law dependence of γ^*; the straight line has gradient 3.

have also been found in molecular dynamics simulations by Toxvaerd and Stecki [43] for a model equimolar binary mixture in which the 11 and 22 potentials are identical, truncated Lennard-Jones, with the 12 potential being purely repulsive. Very recently Chacón *et al* [44] found very pronounced oscillations on the liquid side of the planar liquid–gas interface in Monte Carlo simulations of a liquid–metal described by a pair potential model. In our earlier work on the GCM free interface [11] we addressed the issue of whether capillary-wave fluctuations would destroy the layering structures that we found in the DFT treatment of the interface. The situation for the present model is the same as for the GCM; i.e., we assume that DFT describes the 'bare' or 'intrinsic' profiles—which might be oscillatory, as in the present case—and that fluctuations can be unfrozen on these. If one performs a Gaussian smearing of the profiles over the interfacial thermal roughness $\xi_\perp$ for a density profile with decaying oscillations of wavelength $2\pi/\alpha_1$ and decay length $\tilde{\alpha}_0^{-1}$, these quantities are unaltered but the amplitude is reduced by a factor $\exp[-(\alpha_1^2 - \tilde{\alpha}_0^2)\xi_\perp^2/2]$ [33, 45]. The roughness $\xi_\perp$ depends on the interfacial area L_x^2 and on the external potential, e.g. gravity. Ignoring the latter, one finds that the amplitude of the oscillations in the density profile should be reduced by a factor $(L_x/\xi)^{-\omega[(\alpha_1/\tilde{\alpha}_0)^2-1]}$ where $\omega \equiv (4\pi\beta\gamma\xi^2)^{-1}$ is the standard dimensionless parameter which measures the strength of capillary-wave fluctuations [6] and $\xi \equiv (\tilde{\alpha}_0)^{-1}$. The larger the value of $\omega \propto 1/\gamma^*$, the more damped are the oscillations. The power-law dependence on the interfacial area L_x^2 that this unfreezing procedure predicts is supported by the simulations of Toxvaerd and Stecki [43] and those of Chacón *et al* [44, 46]. For the present model, for states where the oscillations in the DFT profiles are very pronounced, as with the GCM, the calculated exponent in the power law is small, typically -0.1, which implies that the amplitude of the oscillations at these particularly 'stiff' interfaces should only be weakly damped by the capillary-wave fluctuations. As emphasized in [11] the reduced surface tension γ^* far from the critical point is very large in these liquid mixtures, since the coexisting phases correspond to a very high pressure and there are very large density differences, for the individual species, between the phases—see figure 3. Such large values of γ^* do not normally arise at the liquid–

vapour interface of simple, one-component fluids where the solid phase intervenes at low temperatures. However, the model considered by Chacón *et al* [44] is designed to suppress the ratio of the melting temperature T_m to the critical temperature T_c, i.e., $T_m/T_c \lesssim 0.2$, and in these circumstances γ^* can be large and then damping of the oscillations is weak [46].

5. Star polymers at a hard wall: wetting behaviour

By integrating the normal component of the osmotic pressure in the interior of the star polymer along the area of contact between the star and the wall, Jusufi *et al* [21] were able to calculate the force, $F(z)$, and therefore the potential acting between a star polymer and a hard wall, with z denoting the distance from the star centre to the planar wall surface. The force scales as $F(z) \sim 1/z$ as $z \to 0$, and for $z \to \infty$ the form $F(z) \sim (\partial/\partial z)\,\mathrm{erf}(\kappa_i z)$ pertains, where $\mathrm{erf}(x) = (2/\sqrt{\pi})\int_0^x \mathrm{d}t\, \exp(-t^2)$ is the error function and κ_i^{-1} is a length scale of order the radius of gyration of the polymer. For a star polymer with $f = 2$, the value $\kappa_i = 1.16/\sigma_{ii}$ was found to give the best fit to simulations [21]. By matching these two forms at $z = \sigma_{ii}/2$ and then integrating to get the potential, Jusufi *et al* [21] proposed the following form for the effective potential $V_i(z)$ between a star polymer and a hard, planar wall:

$$\beta V_i(z) = \Lambda f^{3/2} \begin{cases} -\ln\left(\dfrac{2z}{\sigma_{ii}}\right) - \left(\dfrac{4z^2}{\sigma_{ii}^2} - 1\right)\left(\psi_i - \dfrac{1}{2}\right) + \zeta_i & \text{for } z \leqslant \sigma_{ii}/2; \\ \zeta_i\, \mathrm{erfc}(\kappa_i z)/\mathrm{erfc}(\kappa_i \sigma_{ii}/2) & \text{for } z > \sigma_{ii}/2, \end{cases} \tag{22}$$

where $\mathrm{erfc}(x) = 1 - \mathrm{erf}(x)$ is the complementary error function, $\psi_i = (1 + \kappa_i^2\sigma_{ii}^2/2)^{-1}$ is a parameter chosen to guarantee the continuity of the local osmotic pressure in the interior of the star polymer and

$$\zeta_i = \frac{2\sqrt{\pi}\psi_i}{\kappa_i\sigma_{ii}}\,\mathrm{erfc}\left(\frac{\kappa_i\sigma_{ii}}{2}\right)\exp\left(\frac{\kappa_i^2\sigma_{ii}^2}{4}\right). \tag{23}$$

The final parameter Λ, which has a weak f-dependence, is also chosen to match the simulation results, giving $\Lambda = 0.46$ when $f = 2$ [21].

By using equation (22) for the external potential in equation (18) we are modelling the binary star-polymer fluid at a hard wall. We found that for certain states approaching the binodal on the side poor in species 1, the larger particles, a thick wetting layer of the coexisting phase rich in species 1 was adsorbed at the wall, the thickness of which diverged at the binodal. Typical wetting density profiles are displayed in figure 7. These were calculated along a constant-density path $\rho\sigma_{11}^3 = 7.0$, approaching the binodal (path A in figure 8). Upon investigating higher total densities we found that there is a first-order wetting transition [47], above which the wall no longer wets completely. The point on the binodal at which the wetting transition occurs, the wetting point, is at $(x, \rho\sigma_{11}^3) = (0.959, 9.15)$. Descending from the wetting point is a short pre-wetting line, ending in a pre-wetting critical point at $(x, \rho\sigma_{11}^3) = (0.951, 8.75)$. The pre-wetting line is displayed in figure 8. This wetting scenario is very similar to that which we found for the binary GCM fluid at a planar wall with a repulsive Yukawa potential mimicking the effective potential between the Gaussian particles and a hard wall [12].

The wetting point and the pre-wetting line were determined by analysing the density profiles and the adsorption of species 1, Γ_1, defined by

$$\Gamma_1 = \int_0^\infty \mathrm{d}z\, (\rho_1(z) - \rho_1), \tag{24}$$

where $\rho_1 = \rho_1(\infty)$, the density of species 1 in the bulk, i.e., far away from the wall. At the pre-wetting line, the adsorption exhibits a discontinuous jump. In figure 9, the adsorption

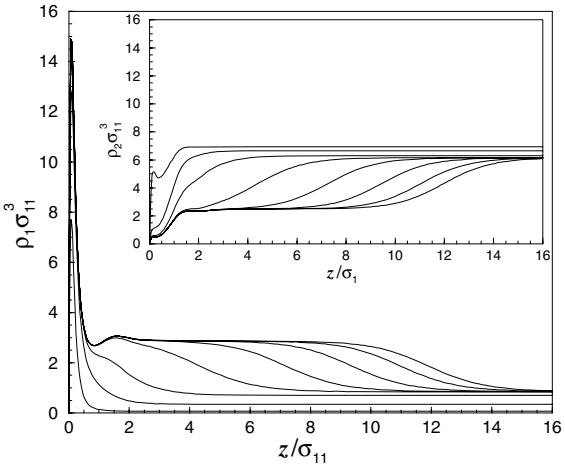

Figure 7. The density profiles of species 1, the larger particles, adsorbed at a wall described by the potential (22), calculated along a path of constant total density, $\rho\sigma_{11}^3 = 7.0$, i.e., path A in figure 8. From left to right the profiles refer to $x = 0.99$, 0.95, 0.9, 0.88, 0.879, 0.878 955, 0.878 951 and 0.878 9505, where x is the concentration of species 2 and $x_{\mathrm{coex}} = 0.878\,950\,19$. The thickness of the adsorbed film increases continuously as $x \to x_{\mathrm{coex}}^+$, indicating complete wetting. The inset shows the density profiles of species 2 for the same values of x. Note that species 2 is depleted from the region adjoining the wall.

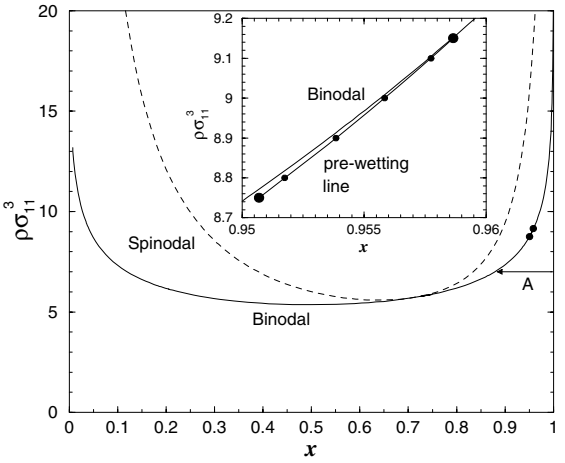

Figure 8. The phase diagram obtained from the RPA (as in figure 3). The two filled circles show the location of the pre-wetting line. The upper point on the binodal is the wetting point where the pre-wetting line meets the binodal tangentially and the lower point is the critical point at the end of the pre-wetting line. The inset shows the pre-wetting line at greater magnification. The horizontal path labelled A is that along which the density profiles in figure 7 are calculated.

calculated along constant-total-density paths ($\rho\sigma_{11}^3 = 9.0$, 8.9, 8.8 and 8.7) approaching the binodal is plotted. Figures 9(a)–(c) correspond to paths that intersect the pre-wetting line, whereas the path of figure 9(d) passes just below the pre-wetting line critical point. We determine the location of the pre-wetting line by monitoring the jump in Γ_1 and, in the region of the pre-wetting critical point, the erosion of two branches in the free energy. On

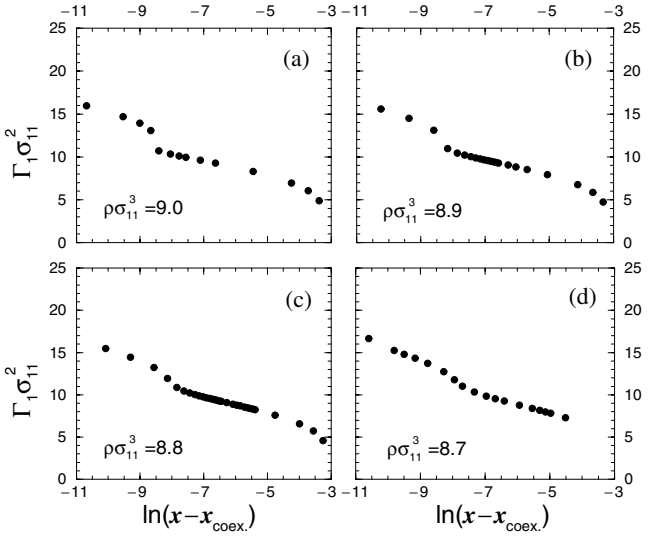

Figure 9. Plots of the adsorption of species 1, Γ_1, versus the logarithm of the deviation from bulk coexistence $\ln(x - x_{\mathrm{coex}})$, at constant total density ρ, for paths intersecting ((a)–(c)) and passing just below (supercritical) (d) the pre-wetting line. The jumps in (a)–(c) indicate the first-order pre-wetting transition.

solving numerically for the density profiles, one moves first along one branch, and then jumps to the other before converging to the equilibrium solution. Note also that the interfacial compressibility, $\chi_{12} = \partial\Gamma_1/\partial\mu_2 \propto (\partial\Gamma_1/\partial x)_\rho$ still has a pronounced peak below the critical point—see figure 9(d). The jump in the adsorption decreases for intersecting paths approaching the pre-wetting critical point. These results should be compared with those of figure 10, where Γ_1 is plotted along the $\rho\sigma_{11}^3 = 7.0$ path (path A in figure 8), along which the density profiles in figure 7 are calculated. This path is far away from the wetting transition, and the film thickness increases smoothly with no jumps as the binodal is approached, the thickness eventually diverging at the binodal.

We find that in the limit $x \to x_{\mathrm{coex}}^+$, below the wetting point Γ_1 increases linearly with $-\ln\Delta x$, where $\Delta x = (x - x_{\mathrm{coex}})$ is the deviation from coexistence. This linear increase with $-\ln\Delta x$ is illustrated in figure 10. For $\Delta x \to 0^+$, Γ_1, as defined by (24), scales proportionally to the film thickness l, i.e., $\Gamma_1 \sim l(\rho_1^{\mathrm{A}} - \rho_1^{\mathrm{B}})$, where ρ_1^{A} is the bulk coexisting density of species 1 in phase A, rich in species 1 and wetting the wall, and ρ_1^{B} is the bulk density in phase B, poor in species 1. Equivalent behaviour was found for the GCM [12] where we were able to describe the results by considering an effective interface potential (excess grand potential per unit) area of the form

$$\Omega_s(l; x) = l(\omega^{\mathrm{A}} - \omega^{\mathrm{B}}) + \gamma_{w,\mathrm{A}} + \gamma_{\mathrm{A,B}} + a\mathrm{e}^{-l/\xi_w} + \mathrm{O}(\mathrm{e}^{-2l/\xi_w}), \tag{25}$$

where $\gamma_{w,\mathrm{A}}$ is the surface tension of the wall–phase A interface, $\gamma_{\mathrm{A,B}}$ that of the free A–B interface, a is a coefficient dependent on ρ and ξ_w is the bulk correlation length in the phase wetting the wall [48–50]. Equation (25) is valid for a complete wetting situation; minimization of Ω_s with respect to l yields the equilibrium film thickness l for a given undersaturation Δx. ω^{B} is the grand potential per unit volume in bulk phase B at given chemical potentials μ_1 and μ_2, while ω^{A} is the corresponding quantity in phase A at the same chemical potentials. To lowest order in the chemical potential deviations,

$$\omega^{\mathrm{A}} - \omega^{\mathrm{B}} \simeq (\rho_1^{\mathrm{A}} - \rho_1^{\mathrm{B}})\,\Delta\mu_1 + (\rho_2^{\mathrm{A}} - \rho_2^{\mathrm{B}})\,\Delta\mu_2. \tag{26}$$

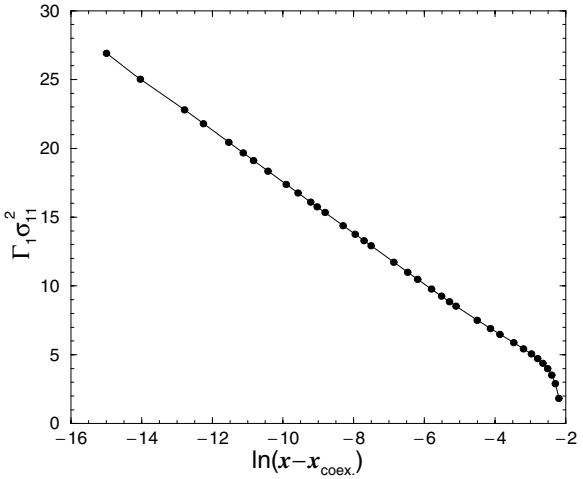

Figure 10. The adsorption of species 1, Γ_1, along path A in figure 8 with constant total density, $\rho\sigma_{11}^3 = 7$, as a function of the logarithm of the deviation from bulk coexistence, $\ln(x - x_{\rm coex})$. The adsorption corresponds to the density profiles in figure 7. On approaching the binodal, Γ_1 increases linearly with $-\ln(x - x_{\rm coex})$.

Since $\Delta\mu_i \equiv (\mu_i - \mu_{i,\rm coex}) \propto \Delta x$ to lowest order, it follows that the first term on the right-hand side of equation (25) is proportional to $l\,\Delta x$. Minimization of equation (25) then yields $l \sim -\xi_w \ln \Delta x$. We were able to confirm that the prefactor to the logarithm is indeed $\xi_w = 1/\alpha_0$, where α_0 is the imaginary part of the pole with the smallest imaginary part (see section 3), in the structure factors, for the bulk wetting phase A.

The wall potential (22) that we employ decays as $\mathrm{erfc}(\kappa_i z) \sim \exp(-\kappa_i^2 z^2)/\sqrt{\pi}\kappa_i z$ as $z \to \infty$. If the wall potential we had chosen had a slower decay, then the effective interface potential (25) might have had additional wall contributions. For example, if the wall potential has an exponential decay of the form $V_i(z) \sim \exp(-z/\lambda)$ as $z \to \infty$, then one needs to add terms of the form $b\exp(-l/\lambda) + \mathrm{O}(\exp(-2l/\lambda))$ to (25) [12, 48, 50]. Then if $\lambda > \xi_w$, we find that minimization of (25) yields $l \sim -\lambda \ln \Delta x$ [12]. Also, equation (25) strictly applies for fluid states where the wetting phase (A) at bulk coexistence lies on the monotonic side of the FW line. This is the case for path A in figure 8. However, if the wetting phase lies on the oscillatory side of the FW line, the term in $\exp(-l/\xi_w)$ should be multiplied by a factor of $\cos(\alpha_1 l + \phi)$, where α_1 is the real part of the dominating pole and ϕ is a phase factor [51].

6. Summary and concluding remarks

We have shown that a binary fluid of star polymers, where the interactions between the star polymers are modelled by purely repulsive effective pair potentials, can phase separate into two fluid phases. When the binodal lies at sufficiently high densities ($\rho\sigma_{11}^3 \gtrsim 5$), the quasi-exact HNC closure to the OZ equations gives results for the bulk structure and thermodynamics (including the binodal) which are very similar to those from the much simpler RPA. We chose pair potential parameters to correspond to a binary fluid of star polymers with $f = 2$ arms with length ratio 2:1 in order to compare with previous results for the binary GCM [11]. The GCM is an effective pair potential between the centres of mass of polymer chains, so on choosing $f = 2$ the star-polymer pair potential should also be that between the central monomers on a pair of polymers. We are therefore comparing two perspectives: 'central monomer' versus 'centre of

mass' as the coordinate for the effective pair potential between the polymers. Since it is the same underlying polymer system that both are describing, the thermodynamics and, therefore, phase diagrams should be similar, and this is indeed what is found. As the structure of the fluid is dependent on the particular 'perspective' that one takes for describing the fluid, one should expect somewhat different structure factors and pair correlation functions. However, the two approaches give a surprisingly similar picture in terms of the location of the FW line relative to the binodal and the values for the bulk correlation length ξ. At this level it appears to matter little that one approach employs an effective pair potential that is finite at $r = 0$ (the GCM) whereas the other has a weakly diverging pair potential (the star polymer). We also found the same line denoting the crossover in the asymptotic decay of the pair correlation functions $h_{ij}(r)$ from damped oscillatory decay with one wavelength to damped oscillatory with another wavelength, joining the cusp in the FW line, that was found for the GCM [11]. By calculating the Lifshitz lines we showed that the location of these is closely related to that of the FW line.

Having shown that the RPA closure is a very good approximation for bulk pair correlation functions, we used the simple Helmholtz free energy functional (7) which generates the RPA to calculate one-body density profiles for the inhomogeneous fluid mixture. In the case of the free fluid–fluid interface the density profiles of both species showed oscillations on both sides of the interface for certain states. The onset of the oscillations was accounted for by the location of the FW line. We also calculated the density profiles of the fluid at a repulsive wall potential equivalent to the effective potential between a star polymer and a hard wall, and showed that there was a first-order wetting transition, with the associated pre-wetting line. The picture that emerged from these studies of the inhomogeneous fluid is very similar to that for the binary GCM [11, 12].

We should comment on how realistic the present approach is for polymer systems. The state-independent pair potential approximation used here is most reliable for modelling polymers in dilute solutions ($\rho\sigma^3 < 1$), and is only approximately correct in the semi-dilute regime [3, 53]. Our results predict demixing phase separation in the semi-dilute regime, in agreement with the results of [54, 55]. In the semi-dilute regime we could expect the log-Gauss (and Gaussian) pair potentials to acquire some additional density-dependence in their parameters, mimicking the effects of many-body forces. Since we have ignored any such dependence in this work, we expect our results to be only semi-quantitatively correct for modelling polymer mixtures in the semi-dilute regime.

The rich bulk and interfacial phenomena displayed by the simple model presented here and in [11, 12] show that the 'colloidal approach' of deriving effective pair potentials between complex polymeric molecules can be very fruitful. Moreover, the remarkable success of the simple and analytically tractable RPA in accounting for bulk correlation functions and thermodynamic properties of the present model opens new perspectives for the study of the properties of inhomogeneous mixtures of such ultrasoft-particle fluids. Given the variety of ways that exist in colloidal science to externally manipulate the conformations of chain-like molecules, we expect the RPA approach to be a tool whose applicability will be much wider than simply to the system of chains in athermal solvents presented here.

Acknowledgments

We thank Gerhard Gompper for bringing [38] to our attention. AJA was supported by an EPSRC studentship.

Appendix

The FTs of the three pair potentials $v_{ij}(r)$ given in equation (1) can be calculated analytically. The pair potentials have the form

$$v_{ij}(r) = \tfrac{5}{18} k_B T f^{3/2}\, F(r/\sigma_{ij};\, \tau_{ij}\sigma_{ij}), \tag{27}$$

with a common function $F(x; y)$ for all combinations $i, j = 1, 2$. Let $Q \equiv k\sigma_{ij}$ and $\bar{\tau}_{ij} \equiv \tau_{ij}\sigma_{ij}$. Equation (27) above implies that the FT $\hat{v}_{ij}(k)$ of the potentials satisfy the relation

$$\hat{v}_{ij}(k) = \tfrac{5}{18} k_B T f^{3/2} \sigma_{ij}^3 \tilde{F}(Q;\, \bar{\tau}_{ij}). \tag{28}$$

Using the specific form of the function $F(x, y)$ given in equation (1) we obtain the function $\tilde{F}(Q; \bar{\tau}_{ij})$ as

$$\begin{aligned}\tilde{F}(Q;\bar{\tau}_{ij}) = {} & \frac{2\pi}{\bar{\tau}_{ij}^2}\left(\frac{\sin Q - Q\cos Q}{Q^3}\right) - 4\pi\left(\frac{\sin Q - \mathrm{Si}(Q)}{Q^3}\right) + \frac{\pi}{\bar{\tau}_{ij}^4}\frac{\sin Q}{Q} \\ & + \frac{1}{2\bar{\tau}_{ij}^2}\left(\frac{\pi}{\bar{\tau}_{ij}^2}\right)^{3/2} \exp[\bar{\tau}_{ij}^2 - Q^2/(4\bar{\tau}_{ij})] \\ & \times \left\{1 - \frac{1}{2}\left[\mathrm{erf}\left(\bar{\tau}_{ij} + \frac{\mathrm{i}Q}{2\bar{\tau}_{ij}}\right) + \mathrm{erf}\left(\bar{\tau}_{ij} - \frac{\mathrm{i}Q}{2\bar{\tau}_{ij}}\right)\right]\right\},\end{aligned} \tag{29}$$

with the sine integral

$$\mathrm{Si}(z) = \int_0^z \frac{\sin t}{t}\,\mathrm{d}t \tag{30}$$

and the complex error function $\mathrm{erf}(z)$. Note that although the arguments of the error functions in equation (29) are complex, the FT is real due to the property $\mathrm{erf}(z^*) = \mathrm{erf}^*(z)$, with the asterisk denoting the complex conjugate [52].

References

[1] Likos C N 2001 *Phys. Rep.* **348** 267
[2] Louis A A, Bolhuis P G, Finken R, Krakoviack V, Meijer E J and Hansen J-P 2002 *Physica* A **306** 251
[3] Bolhuis P G, Louis A A, Hansen J-P and Meijer E J 2001 *J. Chem. Phys.* **114** 4296
[4] Louis A A and Bolhuis P G 2002 *Macromolecules* **35** 1860
[5] Hansen J-P and McDonald I R 1986 *Theory of Simple Liquids* 2nd edn (London: Academic)
[6] Evans R 1992 *Fundamentals of Inhomogeneous Fluids* ed D Henderson (New York: Dekker) ch 3
[7] Grest G S, Fetters L H, Huang J S and Richter D 1996 *Adv. Chem. Phys.* **94** 67
[8] Likos C N, Löwen H, Watzlawek M, Abbas B, Jucknischke O, Allgaier J and Richter D 1998 *Phys. Rev. Lett.* **80** 4450
[9] Watzlawek M, Likos C N and Löwen H 1999 *Phys. Rev. Lett.* **82** 5289
[10] Likos C N and Harreis H M 2002 *Condens. Matter Phys.* **5** 173
[11] Archer A J and Evans R 2001 *Phys. Rev.* E **64** 041501
[12] Archer A J and Evans R 2002 *J. Phys.: Condens. Matter* **14** 1131
[13] A Gaussian effective potential for polymers was first proposed in
Flory P J and Krigbaum J 1950 *Chem. Phys.* **18** 1086
but the model was first studied in detail by
Stillinger F H 1976 *J. Chem. Phys.* **65** 3968
and see also
Stillinger F H and Stillinger D K 1997 *Physica* A **244** 358
[14] Dautenhahn J and Hall C K 1994 *Macromolecules* **27** 5399
[15] Louis A A, Bolhuis P G, Hansen J-P and Meijer E J 2000 *Phys. Rev. Lett.* **85** 2522
[16] Louis A A, Bolhuis P G and Hansen J-P 2000 *Phys. Rev.* E **62** 7961

[17] Lang A, Likos C N, Watzlawek M and Löwen H 2000 *J. Phys.: Condens. Matter* **12** 5087
[18] Likos C N, Lang A, Watzlawek M and Löwen H 2001 *Phys. Rev.* E **63** 031206
[19] Witten T A and Pincus P A 1986 *Macromolecules* **19** 2509
[20] Watzlawek M, Löwen H and Likos C N 1998 *J. Phys.: Condens. Matter* **10** 8189
[21] Jusufi A, Dzubiella J, Likos C N, von Ferber C and Löwen H 2001 *J. Phys.: Condens. Matter* **13** 6177
[22] Dzubiella J, Jusufi A, Likos C N, von Ferber C, Löwen H, Stellbrink J, Allgaier J, Richter D, Schofield A B, Smith P A, Poon W C K and Pusey P N 2001 *Phys. Rev.* E **64** 010401(R)
[23] Finken R, Louis A A and Hansen J-P 2001 *Preprint* cond-mat/0110384
[24] Bhatia A B and Thornton D E 1970 *Phys. Rev.* B **2** 3004
[25] Biben T and Hansen J-P 1991 *Phys. Rev. Lett.* **66** 2215
[26] Likos C N, Hoffmann N, Löwen H and Louis A A 2002 *J. Phys.: Condens. Matter* at press
[27] Louis A A 2001 *Phil. Trans. R. Soc.* A **359** 939
[28] Jusufi A, Watzlawek M and Löwen H 1999 *Macromolecules* **32** 4470
[29] Fishman S and Fisher M E 1981 *Physica* A **108** 1
[30] Belloni L 1993 *J. Chem. Phys.* **98** 8080
[31] Verlet L and Levesque D 1962 *Physica* **28** 1124
[32] Fisher M E and Widom B 1969 *J. Chem. Phys.* **50** 3756
[33] Evans R, Leote de Carvalho R J F, Henderson J R and Hoyle D C 1994 *J. Chem. Phys.* **100** 591
[34] Martynov G A 1992 *Fundamental Theory of Liquids: Methods of Distribution Functions* (Bristol: Hilger)
[35] Evans R, Henderson J R, Hoyle D C, Parry A O and Sabeur Z A 1993 *Mol. Phys.* **80** 755
[36] Leote de Carvalho R J F, Evans R and Rosenfeld Y 1999 *Phys. Rev.* E **59** 1435
[37] Croft L R 2002 private communication
[38] Gompper G and Schick M 1990 *Phys. Rev.* B **41** 9148
[39] Hornreich R M, Liebmann R, Schuster H G and Selke W 1979 *Z. Phys.* B **35** 91
[40] Stephenson J 1970 *J. Math. Phys.* **11** 420
Stephenson J 1970 *Can. J. Phys.* **48** 1724
and
Garel T and Maillard J M 1986 *J. Phys. C: Solid State Phys.* **19** L505
[41] Brader J M, Evans R, Schmidt M and Löwen H 2002 *J. Phys.: Condens. Matter* **14** L1
and see also
Evans R, Brader J M, Roth R, Dijkstra M, Schmidt M and Löwen H 2001 *Phil. Trans. R. Soc.* A **359** 961
[42] Brader J M and Evans R 2000 *Europhys. Lett.* **49** 678
[43] Toxvaerd S and Stecki J 1995 *J. Chem. Phys.* **102** 7163
[44] Chacón E, Reinaldo-Falagán M, Velasco E and Tarazona P 2001 *Phys. Rev. Lett.* **87** 166101
[45] Mikheev L V and Chernov A A 1987 *Zh. Eksp. Teor. Fiz.* **92** 1732 (Engl. transl. 1987 *Sov. Phys.–JETP* **65** 971)
[46] Tarazona P 2002 private communication
[47] A first-order wetting transition and the accompanying pre-wetting were first obtained in
Cahn J W 1977 *J. Chem. Phys.* **66** 3667
and in
Ebner C and Saam W F 1977 *Phys. Rev. Lett.* **38** 1486
[48] See the review by
Dietrich S 1988 *Phase Transitions and Critical Phenomena* vol 12, ed C Domb and J L Lebowitz (London: Academic) p 1
[49] Aukrust T 1987 *PhD Thesis* Institutt for Teoretisk Fysikk Norges Tekniske Hogskole
[50] Aukrust T and Hauge E H 1987 *Physica* A **141** 427
[51] Henderson J R 1995 *Phys. Rev.* E **50** 4836
[52] Abramowitz M and Stegun I A 1965 *Handbook of Mathematical Functions* (New York: Dover)
[53] Bolhuis P G and Louis A A 2002 *Macromolecules* **35** 1860
[54] Broseta D, Leibler L and Joanny J-F 1987 *Macromolecules* **20** 1935
[55] Sariban A and Binder K 1994 *Colloid Polym. Sci.* **272** 1474